

See discussions, stats, and author profiles for this publication at: <https://www.researchgate.net/publication/7329127>

Resonance Raman Study of Bacillus subtilis NO Synthase-like Protein: Similarities and Differences with Mammalian NO Synthases †

ARTICLE *in* BIOCHEMISTRY · MARCH 2006

Impact Factor: 3.02 · DOI: 10.1021/bi051710q · Source: PubMed

CITATIONS

28

READS

22

4 AUTHORS, INCLUDING:



[Dennis J Stuehr](#)

Cleveland Clinic

315 PUBLICATIONS 26,755 CITATIONS

SEE PROFILE

Resonance Raman Study of *Bacillus subtilis* NO Synthase-like Protein: Similarities and Differences with Mammalian NO Synthases[†]

Jérôme Santolini,^{*,‡} Miruna Roman,[‡] Dennis J. Stuehr,[§] and Tony A. Mattioli[‡]

Département de Biologie Joliot-Curie, CEA Saclay, 91191 Gif sur Yvette Cedex, France, and Department of Immunology, Lerner Research Institute, Cleveland Clinic, Cleveland, Ohio 44195

Received August 26, 2005; Revised Manuscript Received December 5, 2005

ABSTRACT: Bacterial NO synthase (NOS)-like proteins such as that from *Bacillus subtilis* (bsNOS) share a high degree of structural homology with the oxygenase domain of mammalian NOSs (mNOSs), but biochemical studies have yet failed to establish that they are specifically capable of producing NO. To better understand the actual function and role of bacterial NOSs, the structure and environment of bsNOS heme were examined with resonance Raman (RR) and ATR-FTIR spectroscopies. We analyzed the structural effects of L-arginine (Arg) and tetrahydrobiopterin (H₄B) binding on several key complexes (ferric, ferrous, ferrous-CO, and ferric-NO) and characterized the bonding properties of the proximal cysteine ligand. While our study fully confirms the similarity between bsNOS and mNOS heme pocket structures, our results also highlight important differences. (i) Contrary to other NOSs, resting native ferric bsNOS exhibits an exclusive five-coordinate high-spin iron status. (ii) The $\nu_{\text{Fe-CO}}$ and ν_{CO} mode frequencies of the bsNOS Fe^{II}CO complexes indicate a weaker electrostatic interaction between Arg and CO. (iii) bsNOS is characterized by a stronger Fe-S bond ($\nu_{\text{Fe-S}} = 342 \text{ cm}^{-1}$), a lower ν_4 frequency, and a negative shift in the $\nu_{\text{Fe-CO}}/\nu_{\text{CO}}$ correlation. (iv) The effects of H₄B on bsNOS heme structure are minor compared to the ones reported on mNOS. These results suggest distinct distal heme environments between mNOS and bsNOS, greater electron-donation properties of bsNOS cysteine proximal ligand, and the absence of a significant influence of H₄B on bsNOS heme properties. These subtle structural differences may reflect changes in the chemistry and physiological role of bacterial NOSs.

Mammalian nitric oxide synthases (NOSs)¹ are multidomain enzymes responsible for the synthesis of NO, which is involved in the regulation of vascular tone, nonspecific immune response, and neuronal communication (1–3). Each

of these activities corresponds to a specific NOS isoform, yet all isoforms exhibit essentially identical crystallographic three-dimensional (3D) structure and chemistry (4, 5). Being heme thiolate proteins with a cysteine as a proximal ligand, NOSs exhibit a P450-like reaction mechanism, albeit adapted to a specific substrate, L-arginine, for producing NO and citrulline (4). In this mechanism, electrons are provided by NADPH and are shuttled through the NOS reductase domain that consists of a two-subunit flavoprotein (4, 6). Electrons are then transferred to the NOS catalytic domain, a heme thiolate subunit, where oxygen activation takes place (7). The oxygenase domain catalyzes two cycles of oxygen activation: (i) the hydroxylation of L-arginine leading to the transient formation of N^ω-hydroxy-L-arginine (NOHA) as an intermediate (8) and (ii) the oxidation of NOHA to produce citrulline and NO (9). In the past few years, NO synthase activity has been found in numerous organisms (10, 11) and particularly in bacteria (12, 13). In parallel, the newly accessible genomes of numerous bacteria have been BLASTed to find novel NO synthases related to mammalian NOSs whose oxygenase domain has been used as a template. Consequently, NOS-like proteins have been cloned in several organisms such as *Deinococcus radiodurans* (14), *Staphylococcus aureus* (15), and *Bacillus subtilis* (16). In addition to the fact that these proteins exhibit a high degree of sequence homology, X-ray crystallography (15, 16) revealed that their 3D structures are extremely similar to the oxygenase domains of mammalian NOS. Because of this high

[†] This work was partly supported by a grant from the Regional Council of the Ile-de-France (T.A.M.).

* To whom correspondence should be addressed: Laboratoire de Biophysique du Stress Oxydant, Département de Biologie Joliot-Curie and CNRS URA 2096, CEA Saclay, 91191 Gif sur Yvette Cedex, France. Telephone: 33-169085363. Fax: 33-169088717. E-mail: jerome.santolini@cea.fr.

[‡] CEA Saclay.

[§] Cleveland Clinic.

¹ Abbreviations: Arg, L-arginine; ATR, attenuated total reflection; DTT, dithiothreitol; EPR, electron paramagnetic resonance; Fe^{II}NO, ferrous heme-nitric oxide complex; Fe^{II}CO, ferrous heme-carbon monoxide complex; Fe^{II}O₂, ferrous heme-oxygen complex; Fe^{III}NO, ferric heme-nitric oxide complex; FTIR, Fourier transform infrared spectroscopy; fwhm, full width at half-maximum; H₄B, tetrahydrobiopterin, (6R)-5,6,7,8-tetrahydro-L-biopterin; Hb, hemoglobin; Mb, myoglobin; HS and LS, high-spin and low-spin, respectively; 6c and 5c, six-coordinate and five-coordinate, respectively; KP_i, inorganic phosphate buffer; NO, nitric oxide; NOHA, N^ω-hydroxy-L-arginine; NOS, nitric oxide synthase; NOS_{oxy}, oxygenase domain of NOS; eNOS, endothelial nitric oxide synthase; iNOS, inducible nitric oxide synthase; mNOS, mammalian nitric oxide synthase; nNOS, neuronal nitric oxide synthase; bsNOS, NOS-like protein isolated from *B. subtilis*; P450_{BM3}, cytochrome P450 CYP102A1 isolated from *Bacillus megaterium*; P450_{cam}, camphor 5-monooxygenase isolated from *Pseudomonas putida*; P450_{sc}, cytochrome P450 in mitochondria of adrenal cortex with cholesterol metabolism activity; P420, thiolate-free coordination of the heme; ROS, reactive oxygen species; RNS, reactive nitrogen species; RR, resonance Raman; saNOS, NOS-like protein isolated from *S. aureus*.

degree of similarity, these new proteins were expected to function like NO synthases. Consistent with this prediction, the *B. subtilis* NOS-like protein (bsNOS) has been shown to exhibit a P450-like reaction mechanism in vitro (17, 18) that leads, under single-turnover conditions, to the biosynthesis of NO.

Nonetheless, it has never been clearly established that these NOS-like proteins are actually capable of producing NO in vivo. Some facts seem to argue against an in vivo NO synthase role. (i) Unlike mammalian NOSs, these bacterial NOSs all lack a "connected" or integral reductase domain required for NOS activity. (ii) Tetrahydrobiopterin (H_4B), an essential cofactor for NOS activity in mammalian NOSs, is presumably absent in the organisms in which NOS-like proteins have been discovered (19). (iii) The net production of NO by these bacterial NOS-like proteins has not been established, yet although these proteins are able to produce nitrite and citrulline in many cases (14, 17), a low level of NO production was only observed in single-turnover conditions (using NOHA instead of Arg as a substrate) with a non-native cofactor (e.g., exogenous H_4B) and with exogenous mammalian NOS reductase proteins (14). (iv) Two different bacterial NOSs from *D. radiodurans* (20) and *Streptomyces turgidiscabies* (21) have been linked to another biological activity, i.e., nitration of amino acids. Thus, despite the similarity of protein sequences, structures, and chemistry between mammalian and bacterial NOSs, biochemical studies failed to prove that these bacterial proteins are bona fide NO synthases.

Key questions related to bacterial NOS-like proteins concern their ability to activate O_2 , the nature of their catalytic mechanism, and thus their precise physiological role. Because of the complexity of the NOS mechanism, subtle changes in heme environment, as well as substrate and cofactor binding sites, could alter NOS chemistry toward new catalytic functions. Therefore, to understand why such structural similarities between mammalian NOSs and their apparent bacterial counterparts lead to functional diversity, a finer and more detailed structure–activity relationship approach is needed. Here, we have used resonance Raman spectroscopy to investigate the structure and probe the physicochemical properties of the heme and its binding pocket in the *B. subtilis* NOS-like protein (bsNOS). This technique is useful in characterizing heme iron spin, oxidation, and coordination states as well as in identifying small differences in heme structure, ligation, conformation, and heme–protein interactions (e.g., H-bonding).

We report here a detailed resonance Raman characterization of bsNOS in the ferric, ferrous, ferrous heme–CO, and ferric heme–NO states in the presence or absence of Arg and/or H_4B . We have specifically examined the effects of Arg and H_4B binding on heme structure, and on heme iron ligand coordination. In addition, we have identified the bsNOS Fe^{III} –S stretching mode and determined its vibrational frequency. Comparison of our results with resonance Raman characterizations of mammalian NOSs and another bacterial NOS (saNOS) reveals subtle structural differences which may reflect differences in the bacterial and mammalian NOS chemistry.

EXPERIMENTAL PROCEDURES

Chemicals. All chemicals were purchased from Sigma or Aldrich (Sigma-Aldrich, St. Louis, MO). NO and CO gases were purchased from Messer (Messer France SA, Asnières, France). NO gas was scrubbed by being flushed through an anaerobic 0.1 M KOH solution. NO-saturated solutions were prepared daily by flushing scrubbed NO gas through a previously degassed 40 mM potassium phosphate (KP_i) buffer at pH 7.4.

Enzyme Preparation. bsNOS and mouse iNOSoxy recombinant proteins were expressed and purified (in the absence of H_4B and Arg) as described previously (17, 22). Samples were incubated in 40 mM KP_i buffer (pH 7.4) in the presence of different combinations of Arg (10 mM) and/or H_4B (400 μ M) and washed by four successive dilution–centrifugation cycles in the final buffer using CentriCon membrane concentrators with a 30 kDa cutoff (Millipore, Bedford, MA). In the case of iNOSoxy, Arg and H_4B binding were verified by UV–visible absorption spectroscopy via the spectral changes of the Soret absorption band from 417 nm (low spin, LS) to 395 nm (high spin, HS). Enzyme concentrations for resonance Raman analysis ranged between 70 and 150 μ M. For samples containing H_4B , DTT was added (final concentration of 3 mM) and a final dilution–concentration cycle with freshly prepared H_4B buffer was performed just before the resonance Raman measurements.

Anaerobic ferric NOS (Fe^{III}) in quartz EPR tubes sealed with airtight rubber septa was prepared directly by 100–200 cycles of alternate vacuum and argon refilling. Ferrous samples (Fe^{II}) were obtained by reduction of Fe^{III} NOS with the addition of a small volume of dithionite solution (5–10 mM) directly into the EPR tube using a gastight syringe (Hamilton, Reno, NV). Ferrous heme–CO ($Fe^{II}CO$) samples were then obtained by flushing CO inside the EPR tube for 10 min to ensure CO saturation of the solution and complete CO binding to Fe^{II} NOS as verified by UV–visible absorption. At the end of the Raman measurement, solutions were transferred into a sealed and degassed optical quartz cuvette and UV–visible absorption spectra were taken to confirm the presence of the $Fe^{II}CO$ adduct. Ferric heme–NO (Fe^{III} –NO) samples were prepared by addition of a small volume of a NO-saturated solution (final concentration of 300 μ M) to the anaerobic ferric NOS solution. The formation and integrity of the complex were verified by resonance Raman spectroscopy and by UV–visible absorption spectra taken at the end of the measurement.

Resonance Raman Spectroscopy. Samples (50 μ L) were placed into a gastight quartz spinning cell, at room temperature, to avoid local heating and to prevent photodissociation and degradation. Raman excitation at 406.7 and 413.1 nm was provided by a krypton ion laser (Spectra-Physics 2000, Spectra-Physics, Mountain View, CA); excitation at 363.8 and 441.6 nm was obtained with an argon ion laser (Coherent Innova 90, Coherent, Santa Clara, CA) and with a He–Cd laser (Kimmon, Tokyo, Japan), respectively. Resonance Raman spectra were recorded using a modified single-stage spectrometer (Jobin-Yvon T64000, Jobin-Yvon, Longjumeau, France) equipped with a liquid N_2 -cooled back-thinned CCD detector. Stray scattered light was rejected using a holographic notch filter (Kaiser Optical Systems, Ann Arbor, MI). Spectra were recorded as the co-addition of 40–240 indi-

vidual spectra with CCD exposure times of 5–30 s each. Three to six successive sets of such spectra were then averaged. Laser power at the sample was <5 mW. Neutral density filters were used for the $\text{Fe}^{\text{II}}\text{CO}$ complexes to decrease laser power (<1 mW) and prevent photodissociation and photooxidation. To accurately determine small frequency differences, the monochromator was calibrated using the excitation wavelength and a saturated sulfate solution; the RR spectra of the samples to be carefully compared were recorded the same day with the same optical geometry, and the spectral precision and accuracy were estimated to be $\pm 1 \text{ cm}^{-1}$. Spectral resolution was $\sim 3 \text{ cm}^{-1}$. Baseline correction was performed using GRAMS 32 (Galactic Industries, Salem, NH).

ATR-FTIR Spectroscopy. Room-temperature FTIR spectra were recorded using a Bruker IFS 66 Fourier transform infrared spectrometer (Bruker Optik GmbH, Ettlingen, Germany) coupled to a single reflection micro ATR prism from Pike Technologies (Madison, WI). Ten microliters of the 500 μM bsNOS $\text{Fe}^{\text{II}}\text{CO}$ sample, prepared as described above, was deposited using a gastight syringe on the ZnSe crystal surface of the ATR unit. The crystal was sealed within a gastight in-house built chamber, which permitted the control of the atmosphere above the sample. Twenty to thirty series of 250 co-added interferograms were averaged for each FTIR measurement. In some cases, a water vapor spectrum was used for background correction. Baseline correction was achieved using GRAMS 32 (Galactic Industries). Each spectrum presented in this work corresponds to the averaging of three to five individual experiments.

Data Analysis. Identification of spectral components in complex unresolved Raman and/or FTIR bands was achieved by the combination of Fourier self-deconvolution and second-order derivative analysis of the averaged spectra: valid peaks were identified when both methods resulted in the same frequency values. In the ν_3 , ν_2 , ν_{vinyl} , γ_{12} , and $\nu_{\text{Fe-CO}}$ regions, overlapping peaks were resolved by fitting, using Origin 6.0 (OriginLab Corp., Northampton, MA), the spectral region to Lorentzian functions for which frequencies were determined by the above Fourier self-deconvolution/second-derivative analysis using GRAMS 32 (Galactic Industries). The NOS Raman bands were assigned following previous assignments on NOS (23–28) and heme proteins (29–32). The determination of the $\nu_{\text{Fe-CO}}$ frequencies by resonance Raman spectroscopy is made difficult by the existence of several $\text{Fe}^{\text{II}}\text{CO}$ species and contributions of other porphyrin modes in the 480–550 cm^{-1} region. The 1900–2000 cm^{-1} spectral region is uncongested and does not contain contributions from the heme porphyrin, protein amide, or C–H or N–H stretching modes (33). Thus, the determination of ν_{CO} mode frequencies in this spectral region is much easier and gives straightforward information about the number and nature of heme pocket conformations. The inverse correlation between the ν_{CO} and $\nu_{\text{Fe-CO}}$ mode frequencies (34) allowed us to exploit the FTIR results to determine the number of corresponding $\nu_{\text{Fe-CO}}$ modes in the RR spectra in the congested region near ca. 500 cm^{-1} and to identify their frequencies.

RESULTS

Characterization of Fe^{III} bsNOS. The UV–visible absorption spectrum of ferric bsNOS (see Figure S1 of the

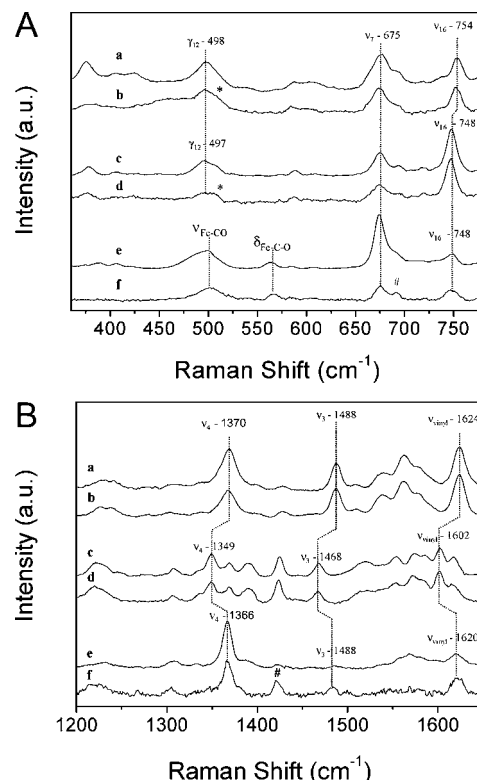


FIGURE 1: Effect of Arg and H_4B binding on bsNOS Fe^{III} , Fe^{II} , and $\text{Fe}^{\text{II}}\text{CO}$ resonance Raman spectra. Panels A and B display the low- and high-frequency regions, respectively, of resonance Raman spectra of bsNOS in the Fe^{III} (a and b), Fe^{II} (c and d), and $\text{Fe}^{\text{II}}\text{CO}$ (e and f) states. Fe^{II} bsNOS was obtained by titration of native bsNOS by addition of a small amount of sodium dithionite. The bsNOS $\text{Fe}^{\text{II}}\text{CO}$ complex was obtained by reduction of native bsNOS under anaerobic conditions followed by 10 min of CO flushing. Excitation wavelengths were 406.7 nm for Fe^{III} bsNOS, 413.1 nm for Fe^{II} bsNOS, and 441.6 nm for $\text{Fe}^{\text{II}}\text{CO}$ bsNOS. bsNOS was analyzed in the absence of Arg and H_4B (a, c, and e) or with both Arg and H_4B (b, d, and f). Dotted lines correspond to frequencies of representative porphyrin and $\text{Fe}^{\text{II}}\text{CO}$ vibrational modes. Asterisks signal the appearance of a shoulder in the γ_{12} region. The number signs denote peaks associated with photodissociation.

Supporting Information), both in the absence and in the presence of Arg and H_4B , exhibits a Soret absorption band at 397 nm indicative of a five-coordinate (5c) high-spin (HS) ferric species; there were no observable traces of a ferric six-coordinate (6c) low-spin (LS) population. This status of the bsNOS heme iron is confirmed by the room-temperature resonance Raman spectra of native bsNOS in the absence of H_4B and Arg, excited at 406.7 nm. The high-frequency region (1300–1700 cm^{-1} , Figure 1Ba and Table 1) exhibits core-size sensitive heme porphyrin modes, which reflect the oxidation, spin, and coordination states of the heme (29): ν_4 (1370 cm^{-1}), ν_3 (1488 cm^{-1}), ν_2 (1562 cm^{-1}), and ν_{vinyl} (1624 cm^{-1}). These frequencies clearly indicate a sole population of bsNOS in the Fe^{III} 5c HS state. In the low-frequency region (Figure 1Aa), the ν_7 , ν_8 , ν_{16} (in-plane porphyrin deformation), and γ_{12} (pyrrole swivel) mode frequencies were observed at 675, 343, 754, and 498 cm^{-1} , respectively. The bsNOS RR spectrum is similar to that observed for cytochromes P450s (30–32), nNOS (23, 25), and saNOS (35) in their ferric high-spin states, but whereas a single high-spin population is observed for saNOS and mNOSs only in the presence of substrate, bsNOS exhibits a

Table 1: bsNOS Fe^{III}, Fe^{II}, Fe^{II}CO, and Fe^{III}NO Resonance Raman Characterization and Effects of Binding of Arginine and H₄B^a

	ν_3	ν_4	ν_2	$\nu_{\text{vinyl}}/\nu_{10}$	ν_7	ν_8	ν_{16}	ν_{33}	γ_{12}
ferric (−/−)	1488	1370	1562	1624/−	675	343	754	—	498
ferric (−/+)	1489	1370	1564	1625/−	675	—	754	458	497/507
ferric (+/−)	1490	1372	1565	1625/−	675	342	755	—	498/510
ferric (+/+)	1486	1369	1561	1623/−	674	—	754	458	497/509
ferrous (−/−)	1468	1349	1572	1617/1602	675	347	748		
ferrous (−/+)	1466	1347	1570	1616/1600	672	344	745		
ferrous (+/+)	1468	1349	1572	1617/1601	676	348	747		

	ν_3	ν_4	ν_2	$\nu_{\text{vinyl}}/\nu_{10}$	ν_7	ν_8	ν_{16}	$\nu_{\text{Fe-CO}}$	$\delta_{\text{Fe-CO}}$	ν_{CO}
Fe ^{II} CO (−/−)	1488	1366	1569	1620/−	674	344	748	485/499	564	1914/1943 ^c
Fe ^{II} CO ^b (−/+)	1467 ^c	1368	nd ^d	1618/1600 ^c	675	344	748	−/502	568	1910 ^c
Fe ^{II} CO ^b (+/−)	1467 ^c	1368	nd ^d	1618/1600 ^c	675	344	749	487/501	567	1917/1933/1944 ^c
Fe ^{II} CO (+/+)	1483	1367	nd ^d	1622/−	675	346	747	−/501	567	1915 ^c

	ν_3	ν_4	ν_2	$\nu_{\text{vinyl}}/\nu_{10}$	ν_7	ν_8	ν_{16}	$\nu_{\text{Fe-NO}}$
Fe ^{III} NO (−/−)	1502	1373	1581	1624/1636	673	342	750	539
Fe ^{III} NO (−/+)	1500	1372	1582	1623/1635	673	342	750	540
Fe ^{III} NO (+/−)	1500	1373	1582	1623/1633	672	345	749	539
Fe ^{III} NO (+/+)	1500	1372	1580	1623/1634	672	341	748	541

^a Frequencies of characteristic heme vibrational modes (in cm^{−1}). Values from the top section were obtained in this report from resonance Raman spectra acquired with laser excitation at 406.7, 441.6, and 413.1 nm (see Experimental Procedures). Abbreviations: (−/−), without H₄B and Arg; (−/+), with only Arg; (+/−), with only H₄B; (+/+), with both H₄B and Arg. ^b Partially dissociated. ^c Ferrous heme modes. ^d Not determined. ^e Values obtained by FTIR.

single ferric high-spin five-coordinate heme state in the rigorous absence of any Arg or H₄B. In the presence of Arg and/or H₄B, the bsNOS Fe^{III} ν_3 , ν_4 , and ν_2 frequencies do not sizably change and remain characteristic of a ferric 5c HS state (Table 1, and Figure S2 of the Supporting Information), indicating no modification of the HS–LS equilibrium. However, Arg and H₄B binding does induce small but significant spectral differences of 2–3 cm^{−1} and the appearance of a prominent shoulder at 507–510 cm^{−1} in the γ_{12} mode region (Figure 1Bb and Table 1). These variations suggest some slight distortion of the heme macrocycle upon Arg and H₄B binding.

Resonance Raman Characterization of iNOSoxy and bsNOS Fe^{III}–S Bond. The Fe–S vibrational mode of iNOSoxy and bsNOS in their Fe^{III} HS state can be examined with RR spectroscopy by exploiting a S → Fe^{III} charge-transfer band, using 363.8 nm excitation (31, 36–38). To discriminate the Fe–S and porphyrin ν_8 modes, which exhibit similar frequencies, we have exploited the differences in the relative enhancements of their RR bands at different excitation wavelengths and in different spin states (LS and HS) (31, 36, 37, 39). We recorded three sets of low-frequency RR spectra: (i) Fe^{III} HS NOS with a Raman excitation wavelength at 406.7 nm (near the Soret absorption band maximum) to preferentially enhance the ν_8 and other porphyrin modes, (ii) Fe^{III} HS NOS with an excitation of 363.8 nm to maximally enhance the Fe–S mode RR band, (iii) 363.8 nm excitation of Fe^{III} LS NOS to abolish HS Fe^{III}–S resonance enhancement. The iNOSoxy Fe^{III} HS state was obtained by addition of saturating concentrations of H₄B and Arg, while the Fe^{III} LS state was obtained in the absence of both H₄B and Arg. For bsNOS, the Fe^{III} HS state is observed in the absence of Arg and H₄B, while Fe^{III} LS bsNOS is obtained upon addition of excess imidazole.

Figure 2A shows these three RR spectra for iNOSoxy. As expected, the porphyrin mode bands at 498, 676, and 754 cm^{−1} change in the relative intensity as the excitation wavelength is changed from 406.7 to 363.8 nm. We

performed a band fitting analysis of the 300–440 cm^{−1} spectral region of these three RR spectra (Figure 2B). The heme porphyrin modes seen at 342, 375, and 403 cm^{−1} with 406.7 nm excitation (Figure 2B, spectrum a) also lose intensity when the RR spectrum is recorded using 363.8 nm excitation (Figure 2B, spectrum b). Also, at this excitation wavelength a new band at 337 cm^{−1} is now resonance-enhanced but that completely disappears for LS Fe^{III} iNOSoxy (Figure 2B, spectrum c). This suggests that the 337 cm^{−1} band is associated with a S → HS Fe^{III} charge-transfer transition, preferentially enhanced for excitation at 363.8 nm excitation (Figure 2B, spectrum b) but absent for the LS Fe^{III} state. We therefore assign the 337 cm^{−1} frequency to the iNOSoxy Fe–S vibrational stretching mode. Similarly, Figure 2C shows the changes in relative intensity of ferric bsNOS porphyrin modes upon changes in excitation wavelength. Figure 2D displays the band-fitting analysis of the 300–440 cm^{−1} spectral region of these spectra. Porphyrin vibrations are observed at 343 and 375 cm^{−1} (Figure 2D, spectrum a), and the Fe–S mode was determined at 342 cm^{−1} (Figure 2D, spectrum b). The two Fe–S frequencies determined here are similar to those reported for the other heme thiolate proteins such as NOS (36), cytochromes P450 (31, 38, 40), and chloroperoxidase (CPO) (37).

Characterization of Fe^{II} and Fe^{II}CO bsNOS Resonance Raman Spectra. The maximum absorption of the bsNOS Fe^{II} complex was found at 412 nm (see Figure S1 of the Supporting Information) that is identical to that which is observed for mammalian NOSs. The room-temperature RR spectra of ferrous bsNOS were thus obtained using excitation at 413.1 nm (Figure 1c,d and Table 1). The ν_4 , ν_3 , and ν_2 mode frequencies observed at 1348, 1468, and 1572 cm^{−1}, respectively, are characteristic of heme thiolate proteins in the 5c HS ferrous state (30), as observed for saNOS (35), P450_{Cam} (30), and nNOS (23). The addition of Arg and H₄B resulted in the appearance of a shoulder in the γ_{12} mode region (around 507 cm^{−1}) and a small decrease of the ν_2 , ν_3 , and ν_{10} frequencies (by −2 cm^{−1}) identical to what we

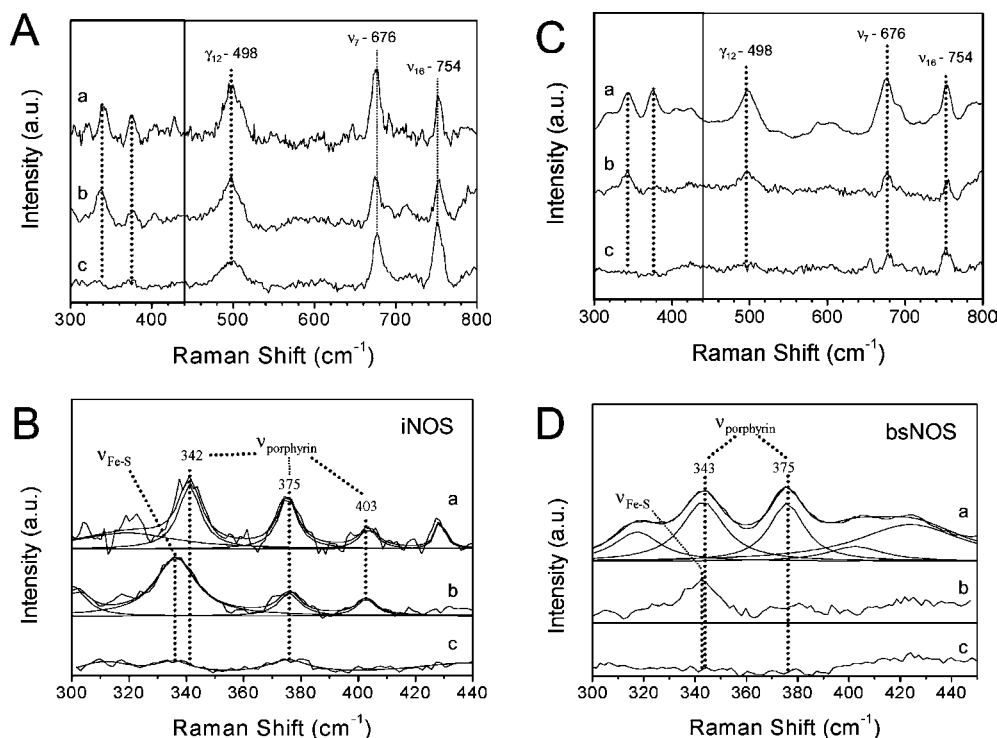


FIGURE 2: Resonance Raman characterization of Fe^{III} iNOSoxy and Fe^{III} bsNOS thiolate proximal ligand. (A) Low-frequency resonance Raman spectra of iNOSoxy with various degrees of porphyrin and proximal ligand Fe^{III}–S vibrational band contributions: (a) iNOSoxy Fe^{III} HS, in the presence of Arg and H₄B, with an excitation wavelength of 406.7 nm, with porphyrin modes preferentially enhanced, (b) iNOSoxy Fe^{III} HS with an excitation wavelength of 363.8 nm, with diminution of the porphyrin mode bands and enhancement of the Fe–S mode band, and (c) iNOSoxy Fe^{III} LS, in the absence of Arg and H₄B, with an excitation wavelength of 363.8 nm, with disappearance of the Fe–S mode band. (B) Fit of the 300–450 cm^{−1} spectral region of iNOSoxy RR spectra (a–c) to a multi-Lorentzian function. (C) Same as panel A for bsNOS. bsNOS HS (a and b) was obtained in the absence of Arg and H₄B; bsNOS Fe^{III} LS (c) was obtained in the presence of imidazole. (D) Same as panel B for bsNOS spectra.

observed for native bsNOS (Figure 1 and Table 1; see Figure S3 of the Supporting Information).

Maximum absorption of the bsNOS Fe^{II}CO complex is observed at 445 nm (see Figure S1 of the Supporting Information). Resonance Raman spectra of this adduct were obtained using an excitation wavelength of 441.6 nm. In the absence of Arg and H₄B, the RR spectrum reflects a 6c LS Fe^{II}CO complex with ν_3 at 1488 cm^{−1}, ν_4 at 1366 cm^{−1}, ν_{vinyl} at 1620 cm^{−1}, ν_2 at 1569 cm^{−1}, and ν_{11} and ν_{37} modes at 1561 and 1581 cm^{−1}, respectively, with no observable bands that could indicate the presence of a ferrous 5c HS heme (Figure 1Be,f and Table 1). This spectrum is similar to those obtained for cytochromes P450s (30–32), CPO (41), and nNOS (23). We observed two new bands at ca. 490 and ca. 560 cm^{−1} (Figure 1Ae). On the basis of extensive analyses of resonance Raman spectra of NOS Fe^{II}CO complexes (25–27, 42), these RR bands can be attributed to the $\nu_{\text{Fe–CO}}$ stretching and $\delta_{\text{Fe–C–O}}$ bending modes, respectively. The addition of Arg and/or H₄B binding had little or no effect on the porphyrin mode frequencies. It only resulted in a slight increase in the level of CO photodissociation as signaled by the appearance of RR bands characteristic of ferrous species (Figure 1Af,Bf and Table 1, and Figure S4 of the Supporting Information) such as 746 cm^{−1} (ν_{16} mode) and 1467 cm^{−1} (ν_3), and an increased intensity at 1428 and 1391 cm^{−1} [characteristic ferrous heme depolarized modes (30)]. This increased extent of photodissociation upon substrate binding is a common phenomenon that has also been observed for cytochromes P450s (32) and NOSs (26). We measured the resonance Raman spectra of the Fe^{III} and

Fe^{II} bsNOS complexes under the same excitation conditions (441.6 nm) and verified that these species contribute negligibly (less than 10%) to the Fe^{II}CO RR signal (data not shown).

As described in the next section, we investigated the effects of Arg and H₄B on bsNOS Fe–C–O frequencies by using an approach combining RR and FTIR spectroscopies to examine both the $\nu_{\text{Fe–CO}}$ and ν_{CO} stretching modes, respectively.

Analysis of $\nu_{\text{Fe–CO}}$ and ν_{CO} of the bsNOS Fe^{II}CO Complex. ATR-FTIR spectra of bsNOS in the presence of different combinations of H₄B and Arg are displayed in Figure 3A. In the absence of Arg and H₄B (Figure 3Aa and Table 1), two ν_{CO} mode bands are observed, a prominent one at 1943 cm^{−1} and a minor one at 1914 cm^{−1}. Addition of H₄B leads to the appearance of a third band around 1933 cm^{−1} (Figure 3Ab and Table 1) and to an increase in the relative intensity of the 1914–1917 cm^{−1} band. Similar FTIR data have been reported for the iNOS Fe^{II}CO complex with ν_{CO} mode frequencies at 1934, 1946, and 1957 cm^{−1} in the absence of Arg (43). This has been interpreted as the existence of two subsets of conformations: (i) a closed conformation that corresponds to a lower CO vibrational frequency and (ii) an open conformation that displays a higher CO frequency. Addition of Arg induces the disappearance of the open conformation, resulting in the observation of only one band corresponding to the closed conformation (at 1915 or 1910 cm^{−1} with or without H₄B, Figure 3Ac,d). This effect has already been observed for iNOS, with a “closed” ν_{CO} frequency of ca. 1905 cm^{−1} (43).

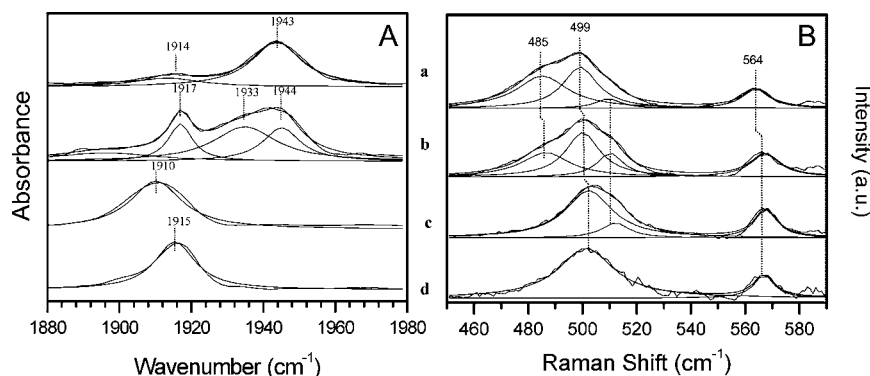


FIGURE 3: Determination of bsNOS ν_{CO} and $\nu_{\text{Fe-CO}}$ stretching frequencies. The bsNOS $\text{Fe}^{\text{II}}\text{CO}$ complex was obtained under anaerobic conditions by titration with sodium dithionite and CO flushing. (A) Determination of the ν_{CO} frequency by ATR-FTIR. Twenty to thirty series of 250 infrared spectra were accumulated and averaged. Background and baseline were corrected on each averaged spectrum. Curves represent the average of three to five series of experiments. Curves were fitted to multi-Lorentzian functions. (B) Determination of the $\nu_{\text{Fe-CO}}$ frequency by resonance Raman spectroscopy. The 450–600 cm^{-1} region of bsNOS $\text{Fe}^{\text{II}}\text{CO}$ resonance Raman spectra (see Figure S4 of the Supporting Information) was fitted to a multi-Lorentzian function. Experiments were achieved in the absence of Arg and H_4B (a), with only H_4B (b), with only Arg (c), or with both Arg and H_4B (d). Dotted lines correspond to the frequencies of $\nu_{\text{Fe-CO}}$ (485 cm^{-1} for the open and 499 cm^{-1} for the closed conformations) and $\delta_{\text{Fe-C-O}}$ (564 cm^{-1}) modes and to porphyrin (ca. 510 cm^{-1}) modes.

Using these FTIR results, we performed a Lorentzian band-fitting analysis of the 460–530 cm^{-1} spectral region of bsNOS $\text{Fe}^{\text{II}}\text{CO}$ resonance Raman spectra (Figure 3B). In the absence of Arg and H_4B , we can identify three different components (Figure 3Ba and Table 1) using second-derivative and Fourier self-deconvolution techniques (see Experimental Procedures): two prominent components are found at 485 and 499 cm^{-1} , corresponding to the aforementioned open and closed conformations, respectively, of the bsNOS $\text{Fe}^{\text{II}}\text{CO}$ complex and a third minor component at ca. 510 cm^{-1} . This latter shoulder has already been observed for nNOS and saNOS and has been proposed to correspond to a porphyrin mode that is enhanced via Fermi resonance coupling (26, 35). Addition of H_4B slightly increases the proportion of the closed conformation without significantly modifying $\nu_{\text{Fe-CO}}$ frequencies that are seen at 487 and 501 cm^{-1} (Figure 3Bb); these observations and conclusions also mirror those from the FTIR data (Figure 3Ab). The addition of Arg (Figure 3Bc,d) suppresses the open conformation without changing the $\nu_{\text{Fe-CO}}$ frequency of the closed conformation (501 or 502 cm^{-1} with or without H_4B , respectively).

Both resonance Raman and FTIR results are coherent and consistent. While the binding of H_4B seems only to be able to slightly increase the relative amount of the closed and open conformations, Arg binding completely suppressed the open conformation. In all cases, Arg or H_4B does not sizably affect the $\nu_{\text{Fe-CO}}$ frequencies of both closed and open conformations. Our results concerning the bsNOS $\text{Fe}^{\text{II}}\text{CO}$ complex are identical to those reported previously for nNOS (26, 27) but differ from what has been described for iNOS and eNOS (27, 42, 44). For iNOS, the high $\nu_{\text{Fe-CO}}$ frequency of the closed conformation (512 cm^{-1}) indicates significantly stronger electrostatic interactions at the CO ligand, presumably with the bound Arg, as compared to bsNOS ($\nu_{\text{Fe-CO}}$ around 500–502 cm^{-1} , this report). Therefore, it appears that, depending on the NOS isoform, the bound Arg substrate can exert different electrostatic effects on the CO ligand.

In parallel, we were able to observe changes in the frequencies of the $\delta_{\text{Fe-C-O}}$ bending mode. In the absence of H_4B and Arg, the $\delta_{\text{Fe-C-O}}$ frequency is found at 564 cm^{-1} (Figure 3B and Table 1). Addition of Arg or H_4B induces a

shift (+3–4 cm^{-1}) of the $\delta_{\text{Fe-C-O}}$ frequency that has been previously described for mammalian NOSs (26) and cytochromes P450 (45) and that most likely reflects a bending of Fe–C–O geometry upon binding of the substrate and/or cofactor (46).

Effect of Arginine and H_4B on bsNOS $\text{Fe}^{\text{III}}\text{NO}$ Coordination. Like those of mNOSs, the $\text{Fe}^{\text{III}}\text{NO}$ bsNOS UV–visible absorption spectrum exhibits a maximum at 436 nm (Figure S1 of the Supporting Information). The resonance Raman spectra of the $\text{Fe}^{\text{III}}\text{NO}$ species were obtained using excitation at 441.6 nm. In the absence of H_4B and Arg, frequencies of porphyrin vibration modes are characteristic of 6c LS $\text{Fe}^{\text{III}}\text{NO}$ species (Figure 4 and Table 1) and are similar to those reported for nNOS and iNOS complexes (24, 28, 42). By analogy with mammalian NOSs (24, 28, 42), the band at 539 cm^{-1} is assigned to the $\nu_{\text{Fe-NO}}$ stretching mode. We did not observe any increase in the level of photooxidation or photodissociation upon binding of Arg or H_4B , nor did we observe any sizable variation in porphyrin mode frequencies (Figure 4 and Table 1). The addition of H_4B resulted in an increase in the relative intensities of the RR bands between 680 and 750 cm^{-1} (Figure 4c,d) in a manner similar to what has been observed for iNOS (42) and which has been interpreted as an increase in heme distortion. H_4B also induces the appearance of a small shoulder in the $\nu_{\text{Fe-NO}}$ region (around 546 cm^{-1}), while we observe a small shift of the $\nu_{\text{Fe-NO}}$ band (+1–2 cm^{-1}) upon Arg binding (Table 1). Because of the overlap of the $\nu_{\text{Fe-NO}}$ and $\delta_{\text{Fe-N-O}}$ bands (47), it is difficult to relate these small changes specifically to changes in $\nu_{\text{Fe-NO}}$ mode frequency or to enhancement of $\delta_{\text{Fe-N-O}}$ band intensity. In any case, the effects of Arg and H_4B binding remain minor and do not provide any evidence of significantly modifying the $\text{Fe}^{\text{III}}\text{NO}$ coordination in bsNOS.

DISCUSSION

Genes encoding NOS-like proteins at the level of the oxygenase domain have recently been identified in several bacterial genomes (19). Sequence alignment (19) and X-ray crystal structure data (15, 16) both indicate strong structural similarities between bacterial and mammalian NO synthases.

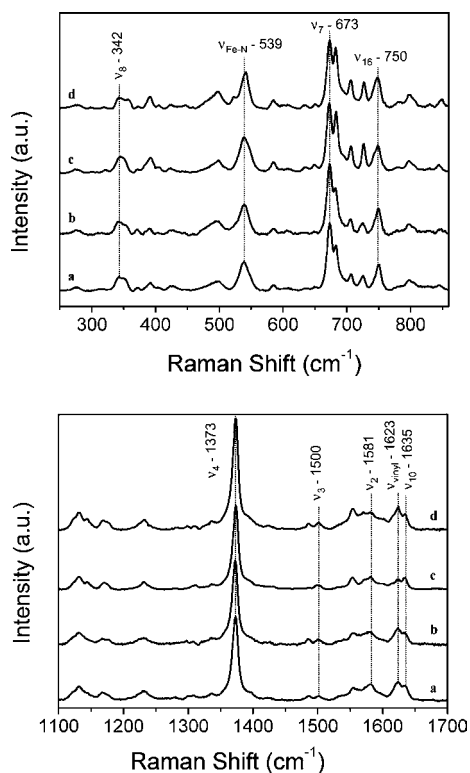


FIGURE 4: Effect of Arg and H₄B binding on the bsNOS Fe^{III}NO resonance Raman spectrum. The Fe^{III}NO bsNOS complex was obtained under anaerobic conditions by addition of small volumes of a NO-saturated solution. The excitation wavelength was 441.6 nm. (A) Low-frequency region of bsNOS Fe^{III}NO complex resonance Raman spectra for different combinations of H₄B and arginine: in the absence of arginine and H₄B (a), with only arginine (b), with only H₄B (c), or in the presence of both Arg and H₄B (d). (B) Same as panel A for the high-frequency region.

Nonetheless, it is not clear yet if bacterial NOSs are capable of producing NO *in vivo*. Therefore, a precise structure–activity relationship study is required to understand the biological role of bacterial NOS. In this paper, we have presented a physical characterization of such a protein from *B. subtilis* using a combination of resonance Raman and ATR-FTIR spectroscopies to determine subtle differences in heme structures, in the Fe–S bond of the heme proximal thiolate ligand, and in the interactions between heme and the protein environment that could reflect particular physicochemical properties of bacterial NOS hemes.

bsNOS and Mammalian NOSs Share Similar Structural Properties. The resonance Raman work presented here confirms that, at the level of the heme and its immediate environment, bsNOS and mammalian NOSs structures are very similar. This resemblance is highlighted by several points. (i) The frequencies of core size sensitive porphyrin modes for the Fe^{III}, Fe^{II}, Fe^{II}CO, and Fe^{III}NO complexes are similar for bsNOS and mNOSs. This suggests a similar heme conformation and analogous heme–protein interactions for bsNOS and mammalian NOSs. (ii) The Fe^{II}–CO, Fe^{III}–NO, and Fe^{III}–S vibrational frequencies are similar for bsNOS, saNOS (35), nNOS (26, 28), eNOS (36), and iNOS (27, 42). This indicates that the modes of coordination of the distal and proximal ligands to bsNOS heme are highly related to those of mNOSs. (iii) The binding of Arg to the bsNOS Fe^{II}–CO complex results in the suppression of the open confor-

mation in favor of the closed conformation, which is similar to what has been reported for mammalian NOSs (26, 27).

Our spectroscopic data confirm the high degree of similarity between bsNOS and mammalian NOS heme general structure. However, this report also stresses specific structural features that could explain differences in bsNOS catalytic properties as compared to its mammalian counterpart.

Variations in the Native NOS Spin State. The nature of the resting, native NOS Fe^{III} spin state and the parameters that control the LS → HS transition are of particular importance in understanding the first catalytic step of NOS. By analogy with P450_{Cam} (48–50), the spin state of native NOSs is believed to be linked to the binding of a water molecule as the sixth ligand of the heme iron. Substrate binding would sterically remove this molecule and promote 6c LS → 5c HS conversion. Because of the high degree of similarity of heme pocket 3D structures as seen by X-ray crystallography (5, 15, 16, 51, 52), all known bacterial and mammalian NOS isoforms were expected to exhibit the same native spin states in the absence of substrate. In fact, in the absence of substrate and cofactor, iNOS appears to be exclusively in a LS state (53, 54); nNOSs, eNOS, and saNOS exhibit a population mixture (80 and 20%) of HS and LS states (35, 55, 56), and in contrast, bsNOS is exclusively 5c HS. The nature of this unusual Fe^{III} spin state for native bsNOS could be related to problems in the accessibility of a water molecule to the distal binding site of the heme. This is seemingly in contradiction with the fact that bacterial NOS sequences lack several N-terminal segments (15–17), which suggests a more open heme pocket structure (15, 16). In fact, we observed, like other groups (17), that native bsNOS was able to bind a sixth ligand such as imidazole and DTT (data not shown). Therefore, the multiplicity of native NOS spin states does not appear to be correlated with changes in accessibility of water at the distal side. By analogy with what has been proposed for P450_{Cam} (49), variations in NOS spin state could be linked to changes in the polarity and/or water content of the heme pocket.

Diversity of the NOS Heme Pocket Environment. For all NOSs, the Fe^{II}CO complex exhibits two distinct conformations, closed and open, the latter being suppressed upon Arg binding. Nonetheless, the ν_{CO} and $\nu_{\text{Fe-CO}}$ mode frequencies vary among NOS isoforms (Table S2 of the Supporting Information). Fe–CO vibrational modes are sensitive to a large extent to electrostatic effects and heme pocket polarity (57). The effect of substrate binding on Fe^{II}CO structure has been correlated to polar factors and has been observed for most of the P450s (45, 58) with some exceptions such as P450_{BM3} (31). A positive electrostatic interaction with the oxygen atom of CO will favor a resonance structure with more Fe^{δ+}=C=O^{δ-} character increasing the Fe–C bond order and decreasing the C–O bond order (57), via electronic back-donation from the Fe $d\pi^*$ orbital to the empty π^* CO orbital. This results in a decrease in the ν_{CO} stretching frequency and an increase in the $\nu_{\text{Fe-CO}}$ stretching frequency (34, 57). This very effect has been observed for iNOS (27, 42). When Arg binds, the positively charged guanidinium group will exert an electrostatic interaction with the oxygen of CO that leads to a strengthening of the Fe–C bond, with an increase in the $\nu_{\text{Fe-CO}}$ frequency up to 511–512 cm^{−1}, and a concomitant weakening of the CO bond, with a decrease in the ν_{CO} frequency down to 1902–1905 cm^{−1}.

(27, 43). The very low observed ν_{CO} frequency and its strong temperature dependence led Jung and colleagues to suggest that a hydrogen bond could be formed between CO and the arginine guanidinium group (43). Comparison of the RR frequencies of $\nu_{\text{Fe-CO}}$ modes for the three mammalian NOS isoforms and two bacterial NOSs (Table S2 of the Supporting Information) when Arg is bound reveals that the frequency observed here for $\text{Fe}^{\text{II}}\text{CO}$ bsNOS ($501\text{--}502\text{ cm}^{-1}$) is similar to that of nNOS (503 cm^{-1}) but significantly lower than that observed for iNOS and eNOS (512 cm^{-1}). This suggests that the effects of the positive guanidinium charge and the strength of the potential H-bond between Arg and CO are weaker in the case of nNOS and bsNOS. This weaker interaction may be due to a screening of the arginine guanidinium positive charge, a longer Arg-CO distance, or a less favorable geometry.

Table S2 of the Supporting Information also reveals that the ν_{CO} frequencies are more similar for Arg-bound $\text{Fe}^{\text{II}}\text{CO}$ iNOS ($1905\text{--}1907\text{ cm}^{-1}$) and $\text{Fe}^{\text{II}}\text{CO}$ bsNOS ($1910\text{--}1915\text{ cm}^{-1}$). Since the ν_{CO} frequencies are similar and the $\nu_{\text{Fe-CO}}$ frequencies are significantly different, these observations may be indicating that the geometry of the Fe-C-O unit (46) may have been altered upon Arg binding. Indeed, a slightly different Arg positioning within the heme distal pocket of nNOS and bsNOS could modify bonding of CO to the heme and increase the Fe-C-O tilt angle. Changes in Arg positioning and heme distal pocket properties could explain the large differences observed in the sensitivity of $\text{Fe}^{\text{II}}\text{CO}$ to substrate binding between iNOS and nNOS/bsNOS. A crystallographic structure of the $\text{Fe}^{\text{II}}\text{CO}$ complex along with a complete characterization of open and closed conformations for all NOSs is required to fully understand this striking difference in NOS diatomic ligand coordination.

Involvement of H_4B in bsNOS Catalysis. H_4B is an important cofactor in mammalian NOSs, acting as both an electron and proton donor during catalytic turnover (59). The production of NO and nitrite by bacterial NOSs seems to depend on, or at least to be enhanced by, the presence of H_4B (14). However, it is generally accepted that H_4B is not present in the organisms in which NOS-like proteins have been found (60). Therefore, the question of the involvement of H_4B or its analogues in bsNOS functioning remains open: either the purported H_4B analogue that is actually involved in bacterial NOS activity has not yet been identified, or the activity of bacterial NOSs that involves H_4B is not physiologically relevant. This report tried to address this question by investigating the influence of H_4B on bsNOS heme structure. The resonance Raman analysis of modifications of NOS porphyrin mode frequencies and distal ligand coordination is a sensitive and powerful method for studying the influence of H_4B binding on the NOS heme pocket (42). Upon addition of H_4B , we observed for ferric bsNOS the appearance of a shoulder in the γ_{12} region along with small shifts in porphyrin vibration frequencies (up to $+2\text{ cm}^{-1}$; Table 1, and Figure S2 of the Supporting Information). Additionally, H_4B addition induced changes in the ν_{CO} and $\nu_{\text{Fe-NO}}$ frequencies (Table 1 and Figures 3 and 4). These effects are reminiscent of those observed for mammalian NOSs (23, 28, 42, 61). But whereas H_4B was reported to induce significant distortion of mNOS heme structure (42), we only observed minor changes in the bsNOS heme RR spectra (Tables S1 and S2 of the Supporting Information).

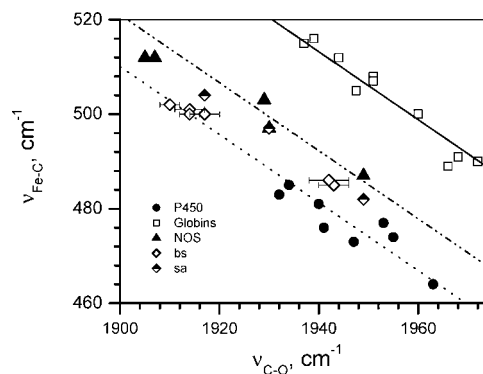


FIGURE 5: Comparison of NOS, globins, P450s, and bsNOS using Fe-C-O stretching modes. $\nu_{\text{Fe-CO}}$ is plotted as a function of ν_{CO} for different $\text{Fe}^{\text{II}}\text{CO}$ complexes of various hemoproteins. Values are derived from the literature (see Table S2 of the Supporting Information) except for bsNOS. Curves (of one protein family) were fitted to a linear function.

Although our results confirm the binding of H_4B near bsNOS heme, once bound, H_4B does not seem to be able to exert the same steric or electrostatic effect on bsNOS heme geometry or ligand coordination as for mammalian NOSs. This suggests that this binding site is not as well-defined as for mammalian NOSs. Consequently, these results provide no strong indication of a possible involvement of H_4B in bsNOS catalysis.

Distinct Properties of the Proximal Cysteine Ligand. Catalytic properties of heme thiolate proteins depend not only on heme conformation and heme pocket environment but also on heme redox properties and the electron density donation properties of the proximal thiolate ligand. This latter effect can be gauged via an analysis of ν_4 porphyrin mode frequencies that reflect the electronic back-donation from an electron-rich axial ligand to the porphyrin π^* antibonding orbitals. ν_4 frequencies are relatively lower for bsNOS ($1369\text{--}1372\text{ cm}^{-1}$) than for mNOS ($1370\text{--}1374\text{ cm}^{-1}$), which suggests that the bsNOS thiolate ligand is a stronger electron donor. The heme proximal bonding can also be investigated via CO coordination. As described above, the π -back-bonding of the $d\pi^*$ Fe electrons into the CO π^* orbitals results in an inverse linear relationship between $\nu_{\text{Fe-CO}}$ and ν_{CO} frequencies (Figure 5). This has been empirically described as $\nu_{\text{Fe-CO}} = 1935 - 0.72\nu_{\text{CO}}$ for globins (34, 46, 57, 62). In parallel, the σ -bonding results in a competition between CO and the proximal ligand for electron density via the iron d_{z^2} orbitals. A strong trans σ -donor, such as thiolate, will therefore weaken the Fe-CO bond and decrease $\nu_{\text{Fe-CO}}$, without affecting the C-O bond. Indeed, the plot of $\nu_{\text{Fe-CO}}$ versus ν_{CO} of NOSs is significantly downshifted to lower $\nu_{\text{Fe-CO}}$ frequencies (Figure 5, $\nu_{\text{Fe-CO}} = 1889 - 0.72\nu_{\text{CO}}$). Cytochromes P450 exhibit even stronger electron-density donation as the $\nu_{\text{Fe-CO}}/\nu_{\text{CO}}$ relationship is further downshifted (Figure 5, $\nu_{\text{Fe-CO}} = 1880 - 0.72\nu_{\text{CO}}$). In this context, the bsNOS $\nu_{\text{Fe-CO}}/\nu_{\text{CO}}$ data seem to fall in a region between those of P450s and mNOSs (Figure 5), which suggests that bsNOS thiolate bonding is stronger than for NOSs but weaker than for P450s. This is confirmed by the bsNOS $\nu_{\text{Fe-S}}$ frequency (342 cm^{-1}) that falls between the $\nu_{\text{Fe-S}}$ frequencies of mNOSs [$337\text{--}338\text{ cm}^{-1}$ (this report and ref 36)] and those of cytochromes P450s [around 351 cm^{-1} (31, 40, 63)]. All these data suggest that the bsNOS thiolate

ligand is a stronger electron donor as compared to mammalian NOSs.

Despite their strong similarities in terms of sequence and 3D structure, our report stresses significant/important variations in heme pocket properties between mammalian and bacterial NOS. We observed significant differences in the thiolate electronic back-donation ("push effect") and in the polarity in the vicinity of the dioxygen ligand ("pull effect"). Moreover, H₄B does not appear to have a well-defined binding site in bsNOS as it does in mammalian NOSs, which suggests that it may not be a bona fide cofactor in bacterial NOSs. All these results could contribute to a re-examination of the chemistry and physiological role of bacterial NOSs.

SUPPORTING INFORMATION AVAILABLE

UV–visible absorption spectra of bsNOS in several oxidation states, resonance Raman spectra of Fe^{III}, Fe^{II}, and Fe^{II}CO bsNOS in the presence or absence of Arg and/or H₄B, and two tables comparing the resonance Raman frequencies of Fe^{III} and Fe^{II}CO complexes between bsNOS and mammalian NOSs in the presence or absence of Arg and/or H₄B. This material is available free of charge via the Internet at <http://pubs.acs.org>.

REFERENCES

- Lincoln, J., Hoyle, C. H. V., and Burnstock, G. (1997) *Nitric Oxide in Health and Disease*, pp 27–133, Cambridge University Press, Cambridge, U.K.
- MacMicking, J., Xie, Q.-W., and Nathan, C. (1997) Nitric oxide and macrophage function, *Annu. Rev. Immunol.* 15, 323–50.
- Cooke, J. P., and Dzau, V. J. (1997) Nitric oxide synthase: Role in the genesis of vascular disease, *Annu. Rev. Med.* 48, 489–509.
- Alderton, W. K., Cooper, C. E., and Knowles, R. G. (2001) Nitric oxide synthases: Structure, function and inhibition, *Biochem. J.* 357, 593–615.
- Fischmann, T. O., Hruza, A., Niu, X. D., Fossetta, J. D., Lunn, C. A., Dolphin, E., Prongay, A. J., Reichert, P., Lundell, D. J., Narula, S. K., and Weber, P. C. (1999) Structural characterization of nitric oxide synthase isoforms reveals striking active-site conservation, *Nat. Struct. Biol.* 6, 233–42.
- Stuehr, D. J., Cho, H. J., Kwon, N. S., Weise, M. F., and Nathan, C. F. (1991) Purification and characterization of the cytokine-induced macrophage nitric oxide synthase: An FAD- and FMN-containing flavoprotein, *Proc. Natl. Acad. Sci. U.S.A.* 88, 7773–7.
- Crane, B. R., Arvai, A. S., Gachhui, R., Wu, C., Ghosh, D. K., Getzoff, E. D., Stuehr, D. J., and Tainer, J. A. (1997) The structure of nitric oxide synthase oxygenase domain and inhibitor complexes, *Science* 278, 425–31.
- Stuehr, D. J., Kwon, N. S., Nathan, C. F., Griffith, O. W., Feldman, P. L., and Wiseman, J. (1991) N^ω-Hydroxy-L-arginine is an intermediate in the biosynthesis of nitric oxide from L-arginine, *J. Biol. Chem.* 266, 6259–63.
- Abu-Soud, H. M., Presta, A., Mayer, B., and Stuehr, D. J. (1997) Analysis of neuronal NO synthase under single-turnover conditions: Conversion of N^ω-hydroxyarginine to nitric oxide and citrulline, *Biochemistry* 36, 10811–6.
- Klessig, D. F., Durner, J., Noad, R., Navarre, D. A., Wendehenne, D., Kumar, D., Zhou, J. M., Shah, J., Zhang, S., Kachroo, P., Trifa, Y., Pontier, D., Lam, E., and Silva, H. (2000) Nitric oxide and salicylic acid signaling in plant defense, *Proc. Natl. Acad. Sci. U.S.A.* 97, 8849–55.
- Golderer, G., Werner, E. R., Leitner, S., Grobner, P., and Werner-Felmayer, G. (2001) Nitric oxide synthase is induced in sporulation of *Physarum polycephalum*, *Genes Dev.* 15, 1299–309.
- Choi, W. S., Seo, D. W., Chang, M. S., Han, J. W., Hong, S. Y., Paik, W. K., and Lee, H. W. (1998) Methyl esters of L-arginine and N-nitro-L-arginine induce nitric oxide synthase in *Staphylococcus aureus*, *Biochem. Biophys. Res. Commun.* 246, 431–5.
- Chen, Y., and Rosazza, J. P. (1995) Purification and characterization of nitric oxide synthase (NOSNoc) from a *Nocardia* species, *J. Bacteriol.* 177, 5122–8.
- Adak, S., Bilwes, A. M., Panda, K., Hosfield, D., Aulak, K. S., McDonald, J. F., Tainer, J. A., Getzoff, E. D., Crane, B. R., and Stuehr, D. J. (2002) Cloning, expression, and characterization of a nitric oxide synthase protein from *Deinococcus radiodurans*, *Proc. Natl. Acad. Sci. U.S.A.* 99, 107–12.
- Bird, L. E., Ren, J., Zhang, J., Foxwell, N., Hawkins, A. R., Charles, I. G., and Stammers, D. K. (2002) Crystal Structure of SANOS, a Bacterial Nitric Oxide Synthase Oxygenase Protein from *Staphylococcus aureus*, *Structure* 10, 1687–96.
- Pant, K., Bilwes, A. M., Adak, S., Stuehr, D. J., and Crane, B. R. (2002) Structure of a nitric oxide synthase heme protein from *Bacillus subtilis*, *Biochemistry* 41, 11071–9.
- Adak, S., Aulak, K. S., and Stuehr, D. J. (2002) Direct evidence for nitric oxide production by a nitric-oxide synthase-like protein from *Bacillus subtilis*, *J. Biol. Chem.* 277, 16167–71.
- Wang, Z. Q., Wei, C. C., Sharma, M., Pant, K., Crane, B. R., and Stuehr, D. J. (2004) A conserved Val to Ile switch near the heme pocket of animal and bacterial nitric-oxide synthases helps determine their distinct catalytic profiles, *J. Biol. Chem.* 279, 19018–25.
- Zemojtel, T., Wade, R. C., and Dandekar, T. (2003) In search of the prototype of nitric oxide synthase, *FEBS Lett.* 554, 1–5.
- Buddha, M. R., Tao, T., Parry, R. J., and Crane, B. R. (2004) Regioselective nitration of tryptophan by a complex between bacterial nitric-oxide synthase and tryptophanyl-tRNA synthetase, *J. Biol. Chem.*
- Kers, J. A., Wach, M. J., Krasnoff, S. B., Widom, J., Cameron, K. D., Bukhalid, R. A., Gibson, D. M., Crane, B. R., and Loria, R. (2004) Nitration of a peptide phytotoxin by bacterial nitric oxide synthase, *Nature* 429, 79–82.
- Ghosh, D. K., Crane, B. R., Ghosh, S., Wolan, D., Gachhui, R., Crooks, C., Presta, A., Tainer, J. A., Getzoff, E. D., and Stuehr, D. J. (1999) Inducible nitric oxide synthase: Role of the N-terminal β -hairpin hook and pterin-binding segment in dimerization and tetrahydrobiopterin interaction, *EMBO J.* 18, 6260–70.
- Wang, J., Stuehr, D. J., Ikeda-Saito, M., and Rousseau, D. L. (1993) Heme coordination and structure of the catalytic site in nitric oxide synthase, *J. Biol. Chem.* 268, 22255–8.
- Wang, J., Rousseau, D. L., Abu-Soud, H. M., and Stuehr, D. J. (1994) Heme coordination of NO in NO synthase, *Proc. Natl. Acad. Sci. U.S.A.* 91, 10512–6.
- Wang, J., Stuehr, D. J., and Rousseau, D. L. (1995) Tetrahydrobiopterin-deficient nitric oxide synthase has a modified heme environment and forms a cytochrome P-420 analogue, *Biochemistry* 34, 7080–7.
- Wang, J., Stuehr, D. J., and Rousseau, D. L. (1997) Interactions between substrate analogues and heme ligands in nitric oxide synthase, *Biochemistry* 36, 4595–606.
- Fan, B., Wang, J., Stuehr, D. J., and Rousseau, D. L. (1997) NO synthase isozymes have distinct substrate binding sites, *Biochemistry* 36, 12660–5.
- Couture, M., Adak, S., Stuehr, D. J., and Rousseau, D. L. (2001) Regulation of the properties of the heme-NO complexes in nitric-oxide synthase by hydrogen bonding to the proximal cysteine, *J. Biol. Chem.* 276, 38280–8.
- Spiro, T. G. (1985) Resonance Raman spectroscopy as a probe of heme protein structure and dynamics, *Adv. Protein Chem.* 37, 111–59.
- Wells, A. V., Li, P., Champion, P. M., Martinis, S. A., and Sligar, S. G. (1992) Resonance Raman investigations of *Escherichia coli*-expressed *Pseudomonas putida* cytochrome P450 and P420, *Biochemistry* 31, 4384–93.
- Deng, T. J., Proniewicz, L. M., Kincaid, J. R., Yeom, H., Macdonald, I. D., and Sligar, S. G. (1999) Resonance Raman studies of cytochrome P450BM3 and its complexes with exogenous ligands, *Biochemistry* 38, 13699–706.
- Tsubaki, M., Hiwatashi, A., and Ichikawa, Y. (1986) Effects of cholesterol and adrenodoxin binding on the heme moiety of cytochrome P-450_{scd}: A resonance Raman study, *Biochemistry* 25, 3563–9.
- Inglelew, W. J., Smith, S. M., Salerno, J. C., and Rich, P. R. (2002) Neuronal nitric oxide synthase ligand and protein vibrations at the substrate binding site. A study by FTIR, *Biochemistry* 41, 8377–84.

34. Ray, G. B., Li, X. Y., Ibers, J. A., Sessler, J. L., and Spiro, T. G. (1994) How Far Can Proteins Bend the Feco Unit: Distal Polar and Steric Effects in Heme-Proteins and Models, *J. Am. Chem. Soc.* 116, 162–76.
35. Chartier, F. J., and Couture, M. (2004) Stability of the heme environment of the nitric oxide synthase from *Staphylococcus aureus* in the absence of pterin cofactor, *Biophys. J.* 87, 1939–50.
36. Schelvis, J. P., Berka, V., Babcock, G. T., and Tsai, A. L. (2002) Resonance Raman detection of the Fe–S bond in endothelial nitric oxide synthase, *Biochemistry* 41, 5695–701.
37. Bangcharoenpaupong, O., Champion, P. M., Hall, K. S., and Hager, L. P. (1986) Resonance Raman studies of isotopically labeled chloroperoxidase, *Biochemistry* 25, 2374–8.
38. Chen, Z. C., Ost, T. W. B., and Schelvis, J. P. M. (2004) Phe393 mutants of cytochrome P450BM3 with modified heme redox potentials have altered heme vinyl and propionate conformations, *Biochemistry* 43, 1798–808.
39. Champion, P. M., Gunsalus, I. C., and Wagner, G. C. (1978) Resonance Raman investigations of cytochrome P450CAM from *Pseudomonas putida*, *J. Am. Chem. Soc.* 100, 3743–51.
40. Champion, P. M., Stallard, B. R., Wagner, G. C., and Gunsalus, I. C. (1982) Resonance Raman detection of an iron–sulfur bond in cytochrome P450cam, *J. Am. Chem. Soc.* 104, 5469–72.
41. Hu, S., and Kincaid, J. R. (1993) Heme active-site structural characterization of chloroperoxidase by resonance Raman spectroscopy, *J. Biol. Chem.* 268, 6189–93.
42. Li, D., Stuehr, D. J., Yeh, S. R., and Rousseau, D. L. (2004) Heme distortion modulated by ligand-protein interactions in inducible nitric-oxide synthase, *J. Biol. Chem.* 279, 26489–99.
43. Jung, C., Stuehr, D. J., and Ghosh, D. K. (2000) FT-Infrared spectroscopic studies of the iron ligand CO stretch mode of iNOS oxygenase domain: Effect of arginine and tetrahydrobiopterin, *Biochemistry* 39, 10163–71.
44. Siddhanta, U., Presta, A., Fan, B., Wolan, D., Rousseau, D. L., and Stuehr, D. J. (1998) Domain swapping in inducible nitric-oxide synthase. Electron transfer occurs between flavin and heme groups located on adjacent subunits in the dimer, *J. Biol. Chem.* 273, 18950–8.
45. Uno, T., Nishimura, Y., Makino, R., Iizuka, T., Ishimura, Y., and Tsuboi, M. (1985) The resonance Raman frequencies of the Fe–CO stretching and bending modes in the CO complex of cytochrome P-450cam, *J. Biol. Chem.* 260, 2023–6.
46. Li, X.-Y., and Spiro, T. G. (1988) Is bound carbonyl linear or bent in heme proteins? Evidence from resonance Raman and infrared spectroscopic data, *J. Am. Chem. Soc.* 110, 6024–33.
47. Hu, S., and Kincaid, J. R. (1991) Resonance Raman characterization of nitric oxide adducts of cytochrome P450cam: The effect of substrate structure on the iron-ligand vibrations, *J. Am. Chem. Soc.* 113, 2843–50.
48. Fisher, M. T., and Sligar, S. G. (1985) Control of heme protein redox potential and reduction rate: Linear free energy relation between potential and ferric spin state equilibrium, *J. Am. Chem. Soc.* 107, 5018–9.
49. Poulos, T. L., Finzel, B. C., and Howard, A. J. (1986) Crystal structure of substrate-free *Pseudomonas putida* cytochrome P-450, *Biochemistry* 25, 5314–22.
50. Sligar, S. G. (1976) Coupling of spin, substrate, and redox equilibria in cytochrome P450, *Biochemistry* 15, 5399–406.
51. Flinspach, M., Li, H., Jamal, J., Yang, W., Huang, H., Silverman, R. B., and Poulos, T. L. (2004) Structures of the Neuronal and Endothelial Nitric Oxide Synthase Heme Domain with D-Nitroarginine-Containing Dipeptide Inhibitors Bound, *Biochemistry* 43, 5181–7.
52. Crane, B. R., Arvai, A. S., Ghosh, D. K., Wu, C., Getzoff, E. D., Stuehr, D. J., and Tainer, J. A. (1998) Structure of nitric oxide synthase oxygenase dimer with pterin and substrate, *Science* 279, 2121–6.
53. Rusche, K. M., Spiering, M. M., and Marletta, M. A. (1998) Reactions catalyzed by tetrahydrobiopterin-free nitric oxide synthase, *Biochemistry* 37, 15503–12.
54. Presta, A., Siddhanta, U., Wu, C., Sennequier, N., Huang, L., Abu-Soud, H. M., Erzurum, S., and Stuehr, D. J. (1998) Comparative functioning of dihydro- and tetrahydropterins in supporting electron transfer, catalysis, and subunit dimerization in inducible nitric oxide synthase, *Biochemistry* 37, 298–310.
55. Rodriguez-Crespo, I., Moenne-Loccoz, P., Loehr, T. M., and Ortiz de Montellano, P. R. (1997) Endothelial nitric oxide synthase: Modulations of the distal heme site produced by progressive N-terminal deletions, *Biochemistry* 36, 8530–8.
56. Gorren, A. C., List, B. M., Schrammel, A., Pitters, E., Hemmens, B., Werner, E. R., Schmidt, K., and Mayer, B. (1996) Tetrahydrobiopterin-free neuronal nitric oxide synthase: Evidence for two identical highly anticooperative pteridine binding sites, *Biochemistry* 35, 16735–45.
57. Li, T. S., Quillin, M. L., Phillips, G. N., and Olson, J. S. (1994) Structural Determinants of the Stretching Frequency of Co Bound to Myoglobin, *Biochemistry* 33, 1433–46.
58. Tsubaki, M., Hiwatashi, A., and Ichikawa, Y. (1987) Effects of cholesterol analogues and inhibitors on the heme moiety of cytochrome P-450scc: A resonance Raman study, *Biochemistry* 26, 4535–40.
59. Wei, C. C., Crane, B. R., and Stuehr, D. J. (2003) Tetrahydrobiopterin radical enzymology, *Chem. Rev.* 103, 2365–83.
60. Raman, C. S., Martasek, P., and Masters, B. S. S. (2000) in *The Porphyrin Handbook* (Guilard, R., Ed.) Academic Press, London.
61. Ingledew, W. J., Smith, S. M., Gao, Y. T., Jones, R. J., Salerno, J. C., and Rich, P. R. (2005) Ligand, Cofactor, and Residue Vibrations in the Catalytic Site of Endothelial Nitric Oxide Synthase, *Biochemistry* 44, 4238–46.
62. Vogel, K. M., Kozlowski, P. M., Zgierski, M. Z., and Spiro, T. G. (1999) Determinants of the FeXO (X = C, N, O) Vibrational Frequencies in Heme Adducts from Experiment and Density Functional Theory, *J. Am. Chem. Soc.* 121, 9915–21.
63. Yoshioka, S., Tosha, T., Takahashi, S., Ishimori, K., Hori, H., and Morishima, I. (2002) Roles of the proximal hydrogen bonding network in cytochrome P450(cam)-catalyzed oxygenation, *J. Am. Chem. Soc.* 124, 14571–9.

BI051710Q